Imperial College London

MSc Applied Mathematics Project

Imperial College London

Department of Mathematics

Numerical methods for a ciliated swimmer and comparison with a squirmer

---

Author:

Hang Su

CID:

01201380

Supervisor:

Dr. Eric E. Keaveny

September 11, 2020

Abstract

Ciliates are micro-organisms covered by numerous hair-like organelles called cilia, which usually exhibit periodic beating patterns. The induced ciliary propulsion was first analysed by Lighthill and Blake, who introduced the concept of 'envelope' to replace the individuality of cilia, and developed the famous squirmer model. However, the difference between the squirmer and a real ciliate remain unclear. In this thesis, we first review interactions of two Lighthill-Blake squirmers. Later, we modify a recently developed multiblob ciliate model that incorporates the distinct ciliary apparatus to analyse the motion of a ciliate. Our numerical results were compared with existing literatures, and verified that the velocity of a spherical ciliate is well predicted by the squirmer model, and that antiplectic metachronal wave is optimal in ciliate swimming speed.

Declarations

The work contained in this thesis is my own work unless otherwise stated.

Signature:

Acknowledgements

Thank you to my supervisor, Eric Keaveny, who is always devoted to thinking and answering my questions. Your expertise was invaluable in the formulating of the research topic.

Thank you to Tim Westwood, who provides so many insights and suggestions, and always offers supports generously.

Thank you to my girlfriend Zishan, for being the light around me during this tough year.

Thanks also to my family, for almost everything.

Contents

List of Figures

List of Tables

Chapter 1

Introduction

1.1 Background

The motion of incompressible viscous fluid is governed by the Navier-Stokes equations, whcih can further be characterised by 'Reynolds number' $Re = \rho U L / \mu$, where ρ is the fluid density, μ the viscosity and U and L are the typical velocity and length scale respectively. From the definition, a low Reynolds number relates to a flow 'slow, small and sticky', called Stokes flow. At low Reynolds number, it is appropriate to study the limit $Re = 0$, which corresponds to a flow of zero inertial effect, and thus the hydrodynamics force experienced by an object must be balanced by any other forces on the object. Setting $Re = 0$ completely removes the time derivative and the inertial term in the Navier-Stokes equations, leaving the great simplification called Stokes equations, featured with instantaneity, linearity and reversibility. The absence of time-derivatives allows the velocity in the flow to be determined instantaneously from the boundary condition and the force, and the linearity relates these relations through a matrix $\mathbf{U} = \mathbf{MF}$, called the mobility problem.

Micro-organisms, as indicated by the name, have small body length and slow swimming speed, and thus live in a world of low Reynolds number. In nature, micro-organisms exhibit different structures and swimming mechanisms. A ciliate, for example, is characterized by the presence of numerous slender organelles called cilia emerging form the cell body, and propels itself through periodic beatings of its cilia. Stated by Purcell's scallop theorem, in order to generate a net displacement of the cell over one period, any periodic motion must be non-reciprocal in time.[Pur77] In the early development, there was lack of technique to analyse a slender cilium. Lighthill and Blake[Bla71] avoided the analysis of individual cilia, and instead introduced a progressive waving envelope that covers the ends of the numerous undulating cilia on the surface to develop the squirmer model, whose motion is mediated by surface squirming instead of ciliary motions. The squirmer model has been used, for example, to analyse the flow field generated by real world

micro-swimmers[GA14][DKPC15], and the interactions of micro-swimmers[ISP06]. However, the differences between the squirmer model and real ciliates remain unclear. Recently, Ito *et al.*[IOI19] developed a ciliate model incorporating the distinct ciliary apparatus, and verified that the swimming speed of a ciliate is well represented by the squirmer model. In the mean time, Schoeller *et al.*[STWK19] developed a flexible filament model, which was incorporated by Westwood[Wes20] in his PhD thesis to construct a ciliated swimmer model.

Both models by Ito *et al.* and Westwood are based on numerical time-integration after solving the linear mobility problem on discrete representation of the ciliate. However, these are two very different models in details, and we summarised here the three most important differences.

1. The entries of the mobility matrix are given by different methods.

   - In Ito *et al.*, the entries are derived from boundary integral method combined with slender-body theory;

   - In Westwood, the entries are given by RPY method[WMZS13].

2. Different actuation of cilia.

   - In Ito *et al.*, the swimming is induced by the prescribed motion of cilia;

   - In Westwood, the ciliary motion is actuated by applying a disturb force at the free end of the cilia, and thus the ciliary motion is undetermined by functional form.

3. Different discretisation of the ciliate.

   - The Ito *et al.* model is discretised using boundary element method;

   - In Westwood the rigid cell body is constructed using multi-blob method[Wes20].

1.2   Objectives and challenges

At the beginning of the project, we received the $C++$ source code of the ciliate model developed by Timothy Westwood. The challenges of this project is for the author to appreciate the existing complex ciliate model and to adapt the prescribed motion described in Ito *et al.*[IOI19] to it, as well as to learn the underlying theories of fluid mechanics. We will also establish the connection and make comparisons between our modified ciliate model and a squirmer.

A large part of this project includes the use of the source code provided by Timothy Westwood. We therefore identify here any source code that is generated by Westwood and any modification to it the author has made.

1. The existing source code being used by the author include:

   - A mathematical class of quaternion to resolve the segment rotations and orientations;

- The construction of tethered filament and rigidbody using multiblob method;

- Numerical solvers for the mobility matrix and time-integration.

2. The modifications by the author include:

- Adapting prescribed ciliary motion to the model, which includes the initialisation method, filament placements, update of the constraint to the base segment and calculations of preferred curvature of the filament;

- The flow field approximation and squirmer speed calculation;

- Any plot and analysis using the generated data.

Other than the ciliate model, the code for the simulation of the interaction of squirmers, i.e. section 3.3 is solely generated by the author.

1.3 Structure of the thesis

In Chapter.2 we outlined any background equations of fluid dynamics that is essential to understand and complete this thesis. While these basic ideas of Stokes flow could be found in most of the modern textbook of fluid mechanics, the equations we used here are largely from the book *A Physical Introduction to Suspension Dynamics*. [GMP11].

In Chapter.3, a brief introduction to the Lighthill-Blake squirmer model is given. Numerical analysis of steady and time-dependent squirmers are performed and compared to existing literatures.

In Chapter.4, we introduced the flexible filament model by Schoeller *et al.*[STWK19], as well as how prescribed motions can be adapted to it. Chapter.4 also includes the simulation of a single filament, and the effect of beat frequency is investigated.

In Chapter.5, the details two different ciliate models are explained.

In Chapter.6, the simulation results of our modified model are presented and compared with that in Ito *et al.*[IOI19]. A comparison is also made to the squirmer model.

Chapter 2

Stokes flow

2.1 Stokes flow equation

The motion of incompressible viscous fluid is governed by the Navier-Stokes equations, i.e. the continuity equation derived from conservation of mass,

$$\nabla \cdot \mathbf{u} = 0, \tag{2.1}$$

and the equation for momentum conservation,

$$\rho \left[\frac{\partial \mathbf{u}}{\partial t} + (\mathbf{u} \cdot \nabla) \mathbf{u} \right] = \mathbf{f} - \nabla p + \mu \nabla^2 \mathbf{u}, \tag{2.2}$$

where $\mathbf{f}$ is the external force density, μ the viscosity, p the pressure and ρ the constant density. The momentum equation can be non-dimensionalised using a typical length scale l and a typical velocity v, leading to a dimensionless equation

$$Re \left[\frac{\partial \mathbf{u}^*}{\partial t^*} + (\mathbf{u}^* \cdot \nabla^*) \mathbf{u}^* \right] = \mathbf{f}^* - \nabla^* p^* + \mu \nabla^{*2} \mathbf{u}^*, \tag{2.3}$$

where the dimensionless Reynolds number is

$$Re = \frac{\rho v l}{\mu}. \tag{2.4}$$

In the limit of zero Reynold's number, the time derivative and the inertia term can be neglected.

The non-linear Navier-Stokes equations simplifies to the Stokes equations,

$$\nabla \cdot \mathbf{u} = 0, \tag{2.5}$$

$$\mathbf{f} - \nabla p + \mu \nabla^2 \mathbf{u} = 0. \tag{2.6}$$

2.2 Fundamental solutions

Since eq.[2.5] is linear, there exist Green's functions. The Green's functions of eq.[2.5] are known as Stokeslet and Rotlet, which assume point forces and torques,

$$\mathbf{u}_s\left(\mathbf{x}; \mathbf{y}, \mathbf{F}\right) = \frac{\mathbf{F}}{8\pi r} + \frac{\left[\mathbf{F} \cdot \left(\mathbf{x} - \mathbf{y}\right)\right]\left(\mathbf{x} - \mathbf{y}\right)}{8\pi r^3} \ (Stokeslet) \tag{2.7}$$

$$\mathbf{u}_r\left(\mathbf{x}; \mathbf{y}, \mathbf{T}\right) = \frac{\mathbf{T} \times \left(\mathbf{x} - \mathbf{y}\right)}{8\pi r^3} \ (Rotlet). \tag{2.8}$$

where $r = |\mathbf{x} - \mathbf{y}|$ and $\mathbf{F}$ and $\mathbf{T}$ represent force and torque applied at $\mathbf{y}$ respectively. Denote $\mathbf{r} = \mathbf{x} - \mathbf{y}$, the relation between $\mathbf{F}$ and $\mathbf{u}_s$ can be expressed by the Oseen tensor

$$G_{ij}(\mathbf{x}, \mathbf{y}) = \frac{1}{8\pi\mu r}\left(\delta_{ij} + \frac{r_i r_j}{r^2}\right) \tag{2.9}$$

such that

$$u_{si} = G_{ij}(\mathbf{x}, \mathbf{y})F_j. \tag{2.10}$$

2.3 Boundary integral method

For an object immersed in a fluid, the velocity field can be constructed using force distribution on this object. Consider a surface S, the velocity field is given by boundary integral equation[Poz92],

$$u_i(\mathbf{x}) = \int_S G_{ij}(\mathbf{x} - \mathbf{y})f_j(\mathbf{y})dS(\mathbf{y}) + \int_S u_j(\mathbf{y})T_{jik}(\mathbf{x} - \mathbf{y})\hat{n}_k(\mathbf{y})dS(\mathbf{y}), \tag{2.11}$$

where $\hat{\mathbf{n}}$ is the outward unit normal, $\mathbf{f}$ is the force density exerted by the surface on the fluid, and T_{ijk} is the stresslet tensor, defined by

$$T_{ijk}(\mathbf{r}) = \frac{-3r_i r_j r_k}{4\pi r}. \tag{2.12}$$

2.4   The general mobility problem

The linearity of eq.[2.5] implies that the transnational and rotational velocities of a particle are related to the forces and torques that it exerts on the fluid,

$$\begin{pmatrix} \mathbf{V} \\ \mathbf{\Omega} \end{pmatrix} = \mathbf{M} \begin{pmatrix} \mathbf{F} \\ \mathbf{T} \end{pmatrix}. \tag{2.13}$$

where $\mathbf{M}$ is the mobility matrix that is in general determined by the geometry of the particle. This relation can be extended to many particles,

$$\begin{pmatrix} \mathbf{V}_1 \\ \vdots \\ \mathbf{V}_N \\ \mathbf{\Omega}_1 \\ \vdots \\ \mathbf{\Omega}_N \end{pmatrix} = \mathbf{M} \begin{pmatrix} \mathbf{F}_1 \\ \vdots \\ \mathbf{F}_N \\ \mathbf{T}_1 \\ \vdots \\ \mathbf{T}_N \end{pmatrix}, \tag{2.14}$$

and $\mathbf{M}$ is determined from the configuration of the particle population.

2.5   Faxén's laws of sphere

Due to linearity, the total hydrodynamic force on a spherical particle can be calculated by summing the force on an inert sphere due to ambient flow and that due to the motion of sphere in a rest fluid.

For a spherical particle of radius a, immersed in a rest fluid at $\mathbf{Y}$, with velocity $\mathbf{U}$ and rotational velocity $\mathbf{\Omega}$, Faxén's laws state that the hydrodynamic force and torque exerted on the particle by the fluid are given by

$$\mathbf{F}_H = 6\pi\mu a \left[\left(1 + \frac{a^2}{6}\nabla^2 \right) \mathbf{u}_{flow}|_{\mathbf{x}=\mathbf{Y}} - \mathbf{U} \right], \tag{2.15}$$

and

$$\mathbf{T}_H = 8\pi\mu a^3 \left[\frac{1}{2} \left(\nabla \times \mathbf{u}_{flow}|_{\mathbf{x}=\mathbf{Y}} \right) - \mathbf{\Omega} \right], \tag{2.16}$$

where $\mathbf{u}_{flow}$ is the external flow due to other particles. eq.[2.15] and eq.[2.16] can be inversed to give

$$\mathbf{U} = -\frac{\mathbf{F}_H}{6\pi\mu a} + \left(1 + \frac{a^2}{6}\nabla^2 \right) \mathbf{u}_{flow}|_{\mathbf{x}=\mathbf{Y}}, \tag{2.17}$$

$$\mathbf{\Omega} = -\frac{\mathbf{T}_H}{8\pi\mu a^3} + \frac{1}{2} \left(\nabla \times \mathbf{u}_{flow}|_{\mathbf{x}=\mathbf{Y}} \right). \tag{2.18}$$

By assuming a force-free and torque-free particle, the force and torque satisfy

$$\mathbf{F}_H + \mathbf{F} = 0, \tag{2.19}$$

$$\mathbf{T}_H + \mathbf{T} = 0 \tag{2.20}$$

where $\mathbf{F}_H$ and $\mathbf{T}_H$ are the hydrodynamic force and torque exerted on the particle by the fluid, and $\mathbf{F}$ and $\mathbf{T}$ denote the total force and torque on the particle from any other sources.

By Newton's third law, the force and torque exerted on the fluid by the particle are

$$-\mathbf{F}_H = \mathbf{F}, \tag{2.21}$$

$$-\mathbf{T}_H = \mathbf{T}, \tag{2.22}$$

which can be inserted in eq.[2.14] and combined with eq.[2.17] and eq.[2.18] to show that for a single spherical particle

$$\mathbf{M} = \begin{pmatrix} \frac{\mathbf{I}}{6\pi\mu a} & \mathbf{0} \\ \mathbf{0} & \frac{\mathbf{I}}{8\pi\mu a^3} \end{pmatrix}, \tag{2.23}$$

where $\mathbf{I}$ is the 3×3 identity matrix.

2.6   The Rotne–Prager–Yamakawa mobility matrix

In the presence of many spherical particles, the Rotne–Prager–Yamakawa method gives explicitly the entries of the mobility matrix [WMZS13]. This method is based on the Faxén's laws explained in section 2.5, and ignores any induced motions due to the presence of other particles.

The RPY mobility matrix for an unbounded fluid is given in the PhD thesis of Timothy Westwood[Wes20]: Consider a population of non-overlapping particles with radius a and let $\mathbf{r}_{nm} = \mathbf{Y}_n - \mathbf{Y}_m$, $r_{nm} = |\mathbf{r}_{nm}| > 2a$ denote their separations from one another. Writing $\hat{\mathbf{r}}_{nm} = \mathbf{r}_{nm}/r_{nm}$ and letting ϵ denote the Levi-Civita symbol in three dimensions, RPY gives the velocities of particle n in an unbounded fluid as

$$\begin{pmatrix} \mathbf{V_n} \\ \mathbf{\Omega_n} \end{pmatrix} = \sum_{m=1}^{N} \begin{pmatrix} \mathbf{M}_{nm}^{tt} & \mathbf{M}_{nm}^{tr} \\ \mathbf{M}_{nm}^{rt} & \mathbf{M}_{nm}^{rr} \end{pmatrix} \begin{pmatrix} \mathbf{F}_m \\ \mathbf{T}_m \end{pmatrix}. \tag{2.24}$$

For $n = m$, the block is the same as eq.[2.23]. For $n \neq m$, the blocks are

$$\mathbf{M}_{nm}^{tt} = \frac{1}{8\pi\mu r_{nm}} \left(\left(1 + \frac{2a^2}{3r_{nm}^2}\right) \mathbf{I} + \left(1 - \frac{2a^2}{r_{nm}^2}\right) \hat{\mathbf{r}}_{nm}\hat{\mathbf{r}}_{nm} \right),$$ (2.25)

$$\mathbf{M}_{nm}^{rr} = \frac{1}{16\pi\mu r_{nm}} \left(3\hat{\mathbf{r}}_{nm}\hat{\mathbf{r}}_{nm} - \mathbf{I}\right),$$ (2.26)

$$\mathbf{M}_{nm}^{tr} = \mathbf{M}_{nm}^{rt} = \frac{1}{8\pi\mu r_{nm}^2} \epsilon \cdot \hat{\mathbf{r}}_{nm}.$$ (2.27)

Chapter 3

The squirmer model

3.1   A solution by Lighthill

In the study of ciliary propulsion, the presence of numerous cilia on the cell body increases the difficulty of analysis. Lighthill and Blake [Lig52] [Bla71] came out with an idea to replace the individuality of the cilia by a progressive waving envelope that covers the ends of the numerous undulating cilia on the surface. Ciliary propulsion is considered generated by the sqirming motion on the envelope, instead of ciliary beating. Such model is termed a 'squirmer'. In this thesis we only consider squirmers of spherical envelope.

Consider a squirmer with orientation $\mathbf{e}$ and radius a placed at the origin. The squirmer is axis-symmetric about its orientation $\mathbf{e}$. The non-slip condition on its surface expresses the squirming motion, and is defined in spherical coordinate, with $\theta = 0$ indicating the orientation $\mathbf{e}$,

$$u_r|_{r=a} = \sum_{n=0}^{\infty} A_n(t) P_n(cos\theta), \tag{3.1}$$

$$u_\theta|_{r=a} = \sum_{n=1}^{\infty}, B_n(t) V_n(cos\theta) \tag{3.2}$$

where P_n is the Legendre polynomial and

$$V_n = \frac{2}{n(n+1)} sin\theta P'_n(cos\theta) = \frac{-2}{n(n+1)} P_n^1(cos\theta), \tag{3.3}$$

with P_n^1 being an associated Legendre function of the first kind. The sets $\mathbf{A} = \{A_n\}$ and $\mathbf{B} = \{B_n\}$ contains the squirming coefficients that define the squirming motion.

With this condition, the solution to the Stokes equation eq.[2.5] is given by [ISP06]

$$\mathbf{u}(\mathbf{x}) = -\frac{1}{3}\frac{a^3}{r^3}B_1\mathbf{e} + B_1\frac{a^3}{r^3}\frac{\mathbf{e}\cdot\mathbf{x}}{r}\frac{\mathbf{x}}{r} + \sum_{n=2}^{\infty}\left(\frac{a^{n+2}}{r^{n+2}} - \frac{a^n}{r^n}\right)B_nP_n(\frac{\mathbf{e}\cdot\mathbf{x}}{r})\frac{\mathbf{x}}{r}$$
$$+ \sum_{n=2}^{\infty}\left(\frac{n}{2}\frac{a^{n+2}}{r^{n+2}} - \left(\frac{n}{2}-1\right)\frac{a^n}{r^n}\right)B_nW_n(\frac{\mathbf{e}\cdot\mathbf{x}}{r})\left(\frac{\mathbf{e}\cdot\mathbf{x}}{r}\frac{\mathbf{x}}{r} - \mathbf{e}\right),$$

(3.4)

where $r=|\mathbf{x}|$ and W_n is defined by

$$W_n(cos\theta) = \frac{2}{n(n+1)}P'_n(cos\theta).$$

(3.5)

The squirming motion induces a movement of the squirmer in the $\mathbf{e}$ direction, with speed given by

$$U = \frac{1}{3}(2B_1 - A_1).$$

(3.6)

In the following analysis, we consider $A_n = 0 \; \forall \; n$ only. That is, the squirmer has only tangential velocity on the envelope. An illustration of the flow induced by such squirmer is shown in Fig.3.1.
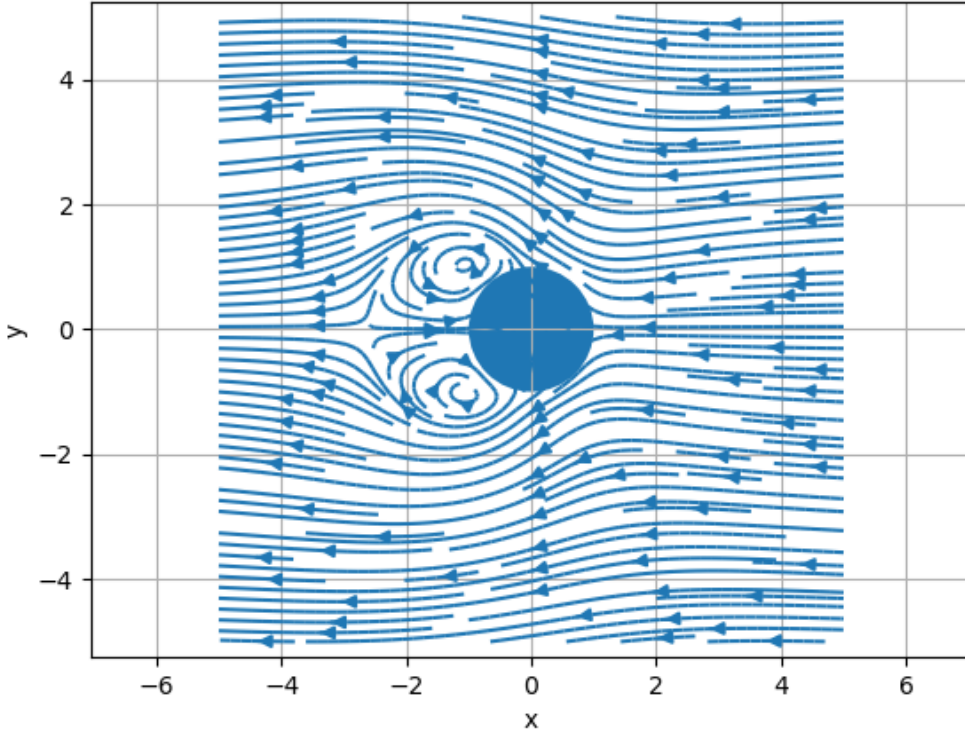

Figure 3.1: The cross section of the 3-D flow of squirming set $\{B_1 = 1, B_2 = 5, A_n = 0 \; \forall \; n\}$, in a frame where the squirmer is stationary. The orientation vector $\mathbf{e}$ is in the positive x-direction.

3.2 Interaction of squirmers

Consider two neutrally buoyant squirmers with the same radius a and squirming set $\mathbf{B}$ in a rest fluid. Denote their positions, velocities, orientations and induced flow field by $\mathbf{X}^{(n)}$, $\mathbf{e}^{(n)}$, $\mathbf{U}^{(n)}$ and $\mathbf{u}_{sol}^{(n)}$ respectively, whith superscripts indicating the squirmer. The linearity of eq.[2.5] implies that the motion of the squirmer 2 is the sum of that due to its squirming motion and that due to the flow induced by squirmer 1 at $\mathbf{X}^{(2)}$.

Since the squirmers considered are spherical and neutrally buoyant, Faxén's laws eq.[2.17] eq.[2.18] apply, and the velocity and rotational velocity of squirmer 2 are given as

$$\mathbf{U}^{(2)} = \frac{2}{3} B_1^{(2)} \mathbf{e}_2 + \left(1 + \frac{a^2}{6} \nabla^2 \right) \mathbf{u}_{sol}^{(1)}|_{\mathbf{x}=\mathbf{X}^{(2)}}, \tag{3.7}$$

$$\mathbf{\Omega}^{(2)} = \frac{1}{2} \left(\nabla \times \mathbf{U}_{sol}^{(1)}|_{\mathbf{x}=\mathbf{X}^{(2)}} \right). \tag{3.8}$$

The equation of motion of squirmer 1 can be obtained by interchanging superscripts (1) and (2) in eq.[3.7] and eq.[3.8].

The presence of many squirmers should alter the unbounded domain solution for a squimrer eq.[3.4], especially when they are close to each other. In addition, when the squirmers are close, they should no longer be treated as a point particle, and the evaluation of flow at their center of mass in invalid. Thus eq.[3.7] and eq.[3.8] only act as far-field approximations to the velocities. More sophisticated calculations and numerical methods have been developed to tackle this near-field motion, including the Boundary element methods Ishikawa *et al.*[ISP06], and the force-coupling method by Keaveny[Kea08].

3.3 Simulation

By numerically integrating eq.[3.7] and eq.[3.8] in time, we here demonstrate the trajectories of two squirmers in a fluid at rest at infinity. In our computations, we discretised time into small time steps. At the start of each time step the translational and angular velocities of squirmers are computed, which are then used to update the positions and orientations of the squirmers. We always normalised the updated orientation vector to keep it unit.

For all simulations, as mentioned earlier we restrict ourselves to the case where the boundary velocity is tangential. In addition to that, only 2-mode squirmer is considered. That is, $A_n = 0 \ \forall \ n$, and $B_n = 0 \ \forall \ n \neq 1, 2$. Therefore only 2 non-zero squirming coefficients B_1 and B_2 are considered. The ratio of B_2 and B_1 is defined as $\beta = B_2/B_1$. In this decomposition, B_1 determines the swimming speed while B_2 determines the stresslet.

(a) Anti-parallel

(b) Parallel
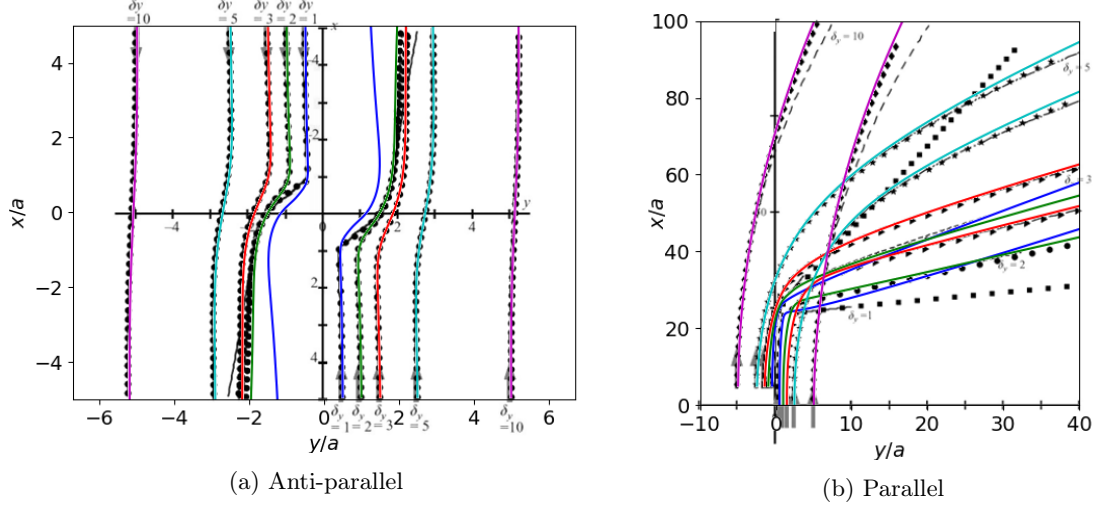
Figure 3.2: Trajectories of two $\beta = 5$ squirmer interactions. Coloured curves express our numerical result, while dashed curves are from Ishikawa *et al.*[ISP06], and symbols are from Keaveny[Kea08]. The initial separations in x-direction are fixed to be 10, and in y-direction are $\delta y = 1, 2, 3, 5$ and 10 respectively. (3.2a): the trajectories of two squirmers initially facing each other. Their starting positions and orientations are indicated by the arrows. (3.2b): trajectories when starting parallel.

3.3.1 Constant B_1 and B_2

Consider first two steady squirmers with constant squirming set $B_1 = 1$ and $B_2 = 5$. Initially, squirmer 2 is placed 10 units of distance from squirmer 1 in the x-direction ($\delta x = 10$). Their separation in the y-direction δy varied from 1 to 10 for different experiments. Their initial orientations are always aligned in the x-direction, either parallel or anti-parallel. The trajectories are shown in Fig.3.2, and are compared with the simulation results in Ishikawa(2006)*et al.*, and Keaveny(2008)*et al.*. Our far-field approximation trajectories are in good agreements with that of more refined simulations, and deviations merely happen at very small proximity when the two squirmers actually collide (trajectories of blue colours in Fig.3.2a. In Fig.3.2b, the deviation at far distance is likely the result of accumulating differences over a long time period.

3.3.2 Time-dependent swimmers

Constant squirming coefficients correspond to a metachronal wave moving restlessly into one direction, which obviously cannot represent a real ciliate. In general the squirming coefficients for real ciliates are time-dependent, and very likely periodic. Recent experiments [GJG10] quantified the periodic swimming gait and resulting flow field of the algae cell *Chlamydomonas Rheinardtii*. The swimming speed and the induced velocity field are fitted by Delmotte *et al.*[DKPC15] to give

a time-dependent squirming set for a 2-mode *C. Rheinardtii* squirmer,

$$B_1(t) = \frac{3}{2}\left(a_0 + a_1 cos(\omega t) + a_2 cos(2\omega t) + b_1 sin(\omega t) + b_2 sin(2\omega t)\right)$$

$$B_2(t) = c_0 + c_1 cos(\omega t + \varphi_{c_1}) + c_2 cos(2\omega t + \varphi_{c_2}) + c_3 cos(3\omega t + \varphi_{c_3}) +$$

$$s_1 sin(\omega t + \varphi_{s_1}) + s_2 sin(2\omega t + \varphi_{s_2}) + s_3 sin(3\omega t + \varphi_{s_3}),$$

(3.9)

where the coefficients and initial phases match the radius of a real cell, are given in Appendix.A. The radius of squirmer is set to be $2.5 \times 10^{-6}m$ and beat frequency $1.89 \times 10^{-4}rad\ s^{-1}$. The average value of $\beta(t)$ over one beat period is given by

$$\bar{\beta} = \frac{1}{T}\int_0^T B_2(y)/B_1(t)dt = 0.1.$$

(3.10)

We examined the trajectories of two interacting *C. Rheinardtii* squirmers and compared it with that of steady squirmers of $\beta = 0.1$. The anti-parallel setup described in section3.3.1 is adopted again, with initial separations $\delta x = 10$ and $\delta y = 2$. Different swimmers are likely to have different phases. We thus added a phase offset $\Delta\varphi \in \{0, 2.75, 5.50\}$ to squirmer 2 than squirmer 1. The trajectories of squirmer 2 for different experiments are shown in Fig.3.3.

We see that the trajectories of a time-varying 2-mode squirmer is well predicted by its average β value. The phase difference produces different terminal orientation and velocity of the squirmer. However, the difference in separation distance of the squirmers is minimal during close-interactions for different $\Delta\varphi$.
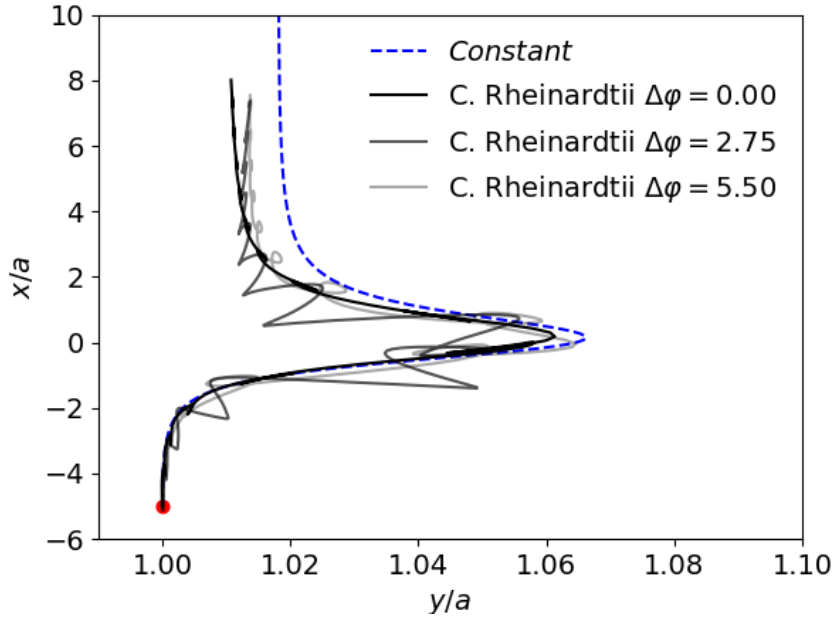

Figure 3.3: Trajectories of one of the *C. Rheinardtii* squirmers. The starting position is indicated by the red dot. The colour depth indicates the starting phase difference of that trajectory. The blue dashed curve is the trajectory of a steady squirmer of $\beta = 0.1$.

Chapter 4

The filament model

The squirmer model of Lighthill and Blake has been widely used to analyse swimming ciliates. However, the role of distinct ciliary apparatus in ciliary propulsion is rarely studied in literature. The mechanics of individual cilia must first be investigated.

4.1   Filament model by Schoeller *et al.*

The cilia can be modelled as flexible filaments that can both bend and twist. Denote a filament length L. At time t, the orientation of the filament at a point is described by the right-handed, orthonormal frame $\{\hat{\mathbf{t}}(s,t), \hat{\mu}(s,t), \hat{\nu}(s,t)\}$, where s is the arclength along the centerline and t is the time. The internal moment experienced by the filament is given by Schoeller *et al.*[STWK19]

$$
\begin{aligned}
\mathbf{M}(s,t) = K_B &\left[\left(\hat{\mathbf{t}} \cdot \frac{\partial \hat{\nu}}{\partial s} - \kappa_{\hat{\mu}}(s,t) \right) \hat{\mu} + \left(\hat{\mu} \cdot \frac{\partial \hat{\mathbf{t}}}{\partial s} - \kappa_{\hat{\nu}}(s,t) \right) \hat{\nu} \right] \\
&+ K_T \hat{\mathbf{t}} \left(\hat{\nu} \cdot \frac{\partial \mu}{\partial s} - \gamma_0(s,t) \right),
\end{aligned}
\tag{4.1}
$$

where K_B and K_T are bending and twisting modulii. Without external forces and torques, the equilibrium shape of the filament is completely determined by the preferred curvatures $\kappa_{\hat{\mu}}$, $\kappa_{\hat{\mu}}$ and a preferred twist γ_0. Thus, we can introduce shape changes of the filament by defining time-dependent $\kappa_{\hat{\mu}}(s,t)$, $\kappa_{\hat{\nu}}(s,t)$ and $\gamma_0(s,t)$.

For a filament immersed in a stokes fluid, the net force and torque on the filament are zero. The force and moment balances are given by

$$
\mathbf{0} = \frac{\partial \mathbf{\Lambda}}{\partial s} + \mathbf{f},
\tag{4.2}
$$

$$
\mathbf{0} = \frac{\partial \mathbf{M}}{\partial s} + \hat{\mathbf{t}} \times \mathbf{\Lambda} + \tau,
\tag{4.3}
$$

where $\mathbf{f}$ and τ are the external force and torque on the filament, and Λ is the internal stress. Denote the position of the centerline on the filament $\mathbf{x}_{cilia}$, the filament must satisfy the kinematic constraint $\hat{\mathbf{t}} = \partial \mathbf{x}_{cilia}/\partial s$. For a tethered filament the boundary condition conditions can be imposed on the position and orientation of the tethered end.

A computational realisation of the filament model [4.1][4.2][4.3] is described in the recent research by Schoeller *et al.* [STWK19]. In their work, the filament is discretised into N segments of same length $\Delta L = L/N$, where each segment is treated as a finite sized particle. Under force-free condition, the hydrodynamic force and torque on the each segment balances its internal stress and moment. The mobility problem left to solve is as described in eq.[2.14]. In their method the RPY mobility matrix is used eq.[2.24], so that the expression on the right hand side of eq.[2.14] is known at all time, and translational and rotational velocities of segments can be solved for. The system is then numerically integrated in time to investigate filament motion.

4.2 Resolving rotation and orientation

Since the flexible filament can twist and bend, each segment is attached with a local orthonormal frame $\{\hat{\mathbf{t}}(s,t), \hat{\mu}(s,t), \hat{\nu}(s,t)\}$, which must also be updated once the translational and rotational velocities are evaluated. The orientation of each local frame obviously cannot be represented by a 3-vector, instead, the advantageous quaternion method is introduced to resolve this problem.[STWK19]

For each segment, there is a unit quaternion $\mathbf{q} = q_0 + q_1\mathbf{i} + q_2\mathbf{j} + q_3\mathbf{k}$ that encodes its orientation. The quaternion can be rewritten as

$$\mathbf{q} = \left(cos\left(\tfrac{\theta}{2}\right), sin\left(\tfrac{\theta}{2}\right)\hat{\mathbf{v}}, \right) \tag{4.4}$$

and can be interpreted as an operator of rotation by angle θ about axis $\hat{\mathbf{v}}$. The corresponding rotation matrix is

$$\mathbf{R}(\mathbf{q}) = \begin{pmatrix} 1 - 2q_2^2 - 2q_3^2 & 2(q_1q_2 - q_3q_0) & 2(q_1q_3 + q_2q_0) \\ 2(q_1q_2 + q_3q_0) & 1 - 2q_1^2 - 2q_3^2 & 2(q_3q_2 - q_1q_0) \\ 2(q_1q_3 - q_2q_0) & 2(q_3q_2 + q_1q_0) & 1 - 2q_2^2 - 2q_1^2 \end{pmatrix}. \tag{4.5}$$

Assume the orientation of a segment is encoded by the quaternion $\mathbf{q}(t)$. Any direction $\mathbf{x}(t)$ that is fixed relative to the particle, i.e. $\mathbf{x}(t) = \hat{\mathbf{t}}(s,t), \hat{\mu}(s,t)$ or $\hat{\nu}(s,t)$, satisfies $\mathbf{x}(t) = \mathbf{R}(\mathbf{q}(t))\mathbf{x}_0$, where $\mathbf{x}(0) = \mathbf{x}_0$ is the initial direction.

When the rotational velocity $\boldsymbol{\Omega}$ is evaluated, the quaternion satisfies the relation

$$\frac{d\mathbf{q}}{dt} = \frac{1}{2}(0, \boldsymbol{\Omega}) \bullet \mathbf{q}. \tag{4.6}$$

The ODE in eq.[4.6] can be solved by numerical method. However, to avoid unnecessary numerical error, Schoeller et $al.$[STWK19] develops a method by introducing a Lie algebra elements $\mathbf{u}$ to update $\mathbf{q}$ in a multiplicative way

$$\mathbf{q}(t_0 + \Delta t) = exp(\mathbf{u}((t_0 + \Delta t), \mathbf{q}(t_0 + \Delta t))) \bullet \mathbf{q}(t_0), \tag{4.7}$$

where the update quaternion is

$$exp(\mathbf{u}) = \left(cos\left(\frac{|\mathbf{u}|}{2}\right), sin\left(\frac{|\mathbf{u}|}{2}\right)\frac{\mathbf{u}}{|\mathbf{u}|} \right). \tag{4.8}$$

The vector $\mathbf{u}$ is updated through

$$\frac{d\mathbf{u}}{dt} = \mathbf{D}_{\mathbf{u}}^{-1}\boldsymbol{\Omega}, \tag{4.9}$$

where $\mathbf{D}_{\mathbf{u}}^{-1}$ is a matrix defined as

$$\mathbf{D}_{\mathbf{u}}^{-1} = \mathbf{I} - \frac{1}{2}[\mathbf{u}\times] - \frac{1}{2|\mathbf{u}|^2}\left(|\mathbf{u}|cot\left(\frac{|\mathbf{u}|}{2}\right) - 2 \right)[\mathbf{u}\times]^2, \tag{4.10}$$

with $[\mathbf{u}\times]$ being the skew-symmetric matrix of $\mathbf{u}$. The problem of updating the unit quaternions $\mathbf{q}$ is now transferred to one of updating the Lie algebra elements $\mathbf{u}$.
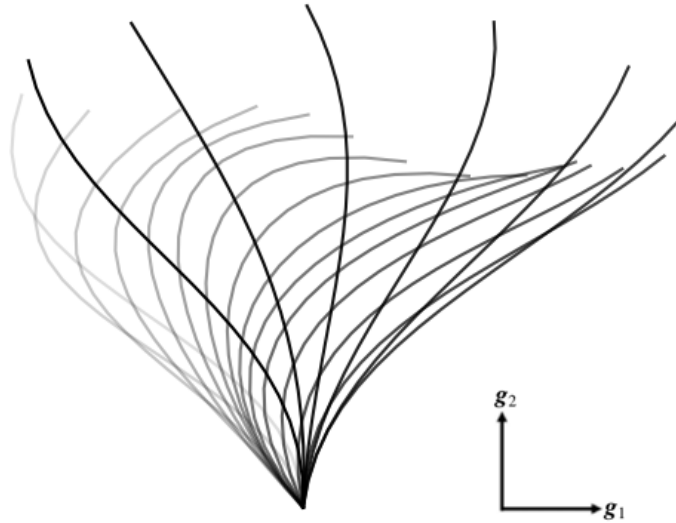
4.3   Prescribed filament motion

Figure 4.1: Ciliary motion during one beat period. Color depths represent the elapsed time.

In the existing computational model, the filament motion is actuated by applying a disturb force

at the free end of the filament, and thus the motion is undetermined by functional form. In order to compare with existing literatures, it is essential to prescribe the motion of filament. Denote $\mathbf{x}_{cilia}$ the positions on the centerline of the filament, $\mathbf{g}_1$ and $\mathbf{g}_2$ the orthonormal basis vectors as shown in Fig.4.1, we adopt a planer filament motion described by the mathematical formula in Fulford & Blake [FB86],

$$\mathbf{x}_{cilia}(s,t) = \xi^{(1)}(s,t)\mathbf{g}_1 + \xi^{(2)}(s,t)\mathbf{g}_2, \tag{4.11}$$

where

$$\xi^{(i)}(s,t) = \frac{1}{2}\alpha_0^{(i)}(s) + \sum_{n=1}^{N_0} \alpha_n^{(i)}(s)\cos(n\omega t) + \beta_n^{(i)}\sin(n\omega t), \tag{4.12}$$

where ω is the beat freqeuncy. The Fourier coefficients $\alpha_n^{(i)}$ and $\beta_n^{(i)}$ are given by

$$\alpha_n^{(i)} = \sum_{m=1}^{3} A_{mn}^{(i)}s^m, \ \beta_n^{(i)} = \sum_{m=1}^{3} B_{mn}^{(i)}s^m, \tag{4.13}$$

with the coefficients $A_{mn}^{(i)}$ and $B_{mn}^{(i)}$ given in Table [B.1] in Appendix.B. In the original paper[IOI19], the values of $A_{mn}^{(i)}$ and $B_{mn}^{(i)}$ correspond to a filament of unit length[1]. The schematics of the filament motion described by eq.[4.11] is shown in Fig.4.1.

4.4 Application to the filament model

4.4.1 Computing preferred curvatures

There is no direct method to apply the mathematical formula eq.[4.11] to the flexible filament model described in section.4.1. However, in the absence of applied force, the equilibrium shape of the filament is determined by preferred curvatures $\hat{\mu}$, $\hat{\nu}$ and twist γ_0 in eq.[4.1]. One can then consider updating $\hat{\mu}$, $\hat{\nu}$ and γ_0 to match the equilibrium shape with the functional shape of eq.[4.11]. The drawback is that the equilibrium shape is not instantaneously achieved. However, in the limit of low beat frequency ω, the functional shape should be well captured by our filament model.

Since the filament motion described by [4.11] is planar, without lost of generality we can place the local basis vectors $\hat{\nu}$ and $\hat{\mathbf{t}}$ of all segments in the plane formed by $\mathbf{g}_1$ and $\mathbf{g}_2$, so that calculating $\kappa_{\hat{\mu}}$ alone is enough to describe the equilibrium shape, and $\kappa_{\hat{\nu}}$ and γ_0 are both zero. In this case, $\kappa_{\hat{\mu}}$ is equal to the curvature of the parametric function [4.11], and is given by

$$\kappa_{\hat{\mu}} = \frac{\xi^{(1)'}\xi^{(2)'} - \xi^{(2)'}\xi^{(1)'}}{\left(\xi^{(1)'^2} + \xi^{(2)'^2}\right)^{\frac{3}{2}}}, \tag{4.14}$$

where

$$\xi^{(i)'} = \frac{\partial\xi^{(i)}}{\partial s} = \frac{1}{2}\alpha_0^{(i)'} + \sum_{n=1}^{N_0}\alpha_n^{(i)'}\cos(n\omega t) + \beta_n^{(i)'}\sin(n\omega t), \tag{4.15}$$

---

[1]This is not quite true. Explanations will be given in section4.4.1

$$\alpha_n^{(i)'} = \frac{\partial \alpha_n^{(i)}}{\partial s} = \sum_{m=1}^{3} m A_{mn}^{(i)} s^{m-1}, \ \beta_n^{(i)'} = \frac{\partial \beta_n^{(i)}}{\partial s} = \sum_{m=1}^{3} m B_{mn}^{(i)} s^{m-1}. \tag{4.16}$$

Since the curvature is equal to the inverse of the radius of the osculating circle, $\kappa_{\hat{\mu}}|_{L=1}$ calculated by eq.[4.14] for a unit filament can be easily scaled as $\kappa_{\hat{\mu}}|_L = (\kappa_{\hat{\mu}}|_{L=1})/L$ to get the correct curvature for a filament of length L.

The discretisation of filament requires only finite number of $\kappa_{\hat{\mu}}$ to be calculated. In the existing source code, $\kappa_{\hat{\mu}}$ is accepted as an input at the joint of any two adjacent segments. Since all segments are of the same length $\Delta L = L/N$, $\kappa_{\hat{\mu}}$ should be evaluated at a set of points of constant separation ΔL on the analytic curve eq.[4.11]. Since eq.[4.11] is parameterised in arclength, it seems $\kappa_{\hat{\mu}}$ can be conveniently evaluated using an equally spaced parameter set $\mathbf{S} = \{\frac{1}{N}, \frac{2}{N}, ..., \frac{(N-1)}{N}\}$, where N is the number of segments in each filament.

However, in practise, we found that since a truncated Fourier series is used in eq.[4.13], the parameter s in eq.[4.11] does not represent the actual arclength, but becomes a general parameter. We verified that the norm of the tangent to eq.[4.11] is not equal to 1, and thus eq.[4.11] must not be parameterised in arclength.

Theorem 1. *For a function parameterised in arclength, the norm of its tangent at any point is equal to 1.*

Proof. Define a parametrisation $\mathbf{X}(t) = (x_1(t), x_2(t), ..., x_n(t))$, where $x_n(t)$ are real-valued differentiable functions. Let $\acute{}$ denotes differentiation with respect to t, the arclength by definition is

$$ds = |\frac{d\mathbf{X}}{dt}| dt = |\dot{\mathbf{X}}| dt = \sqrt{\dot{x}_1^2 + \dot{x}_2^2 + ... + \dot{x}_n^2} dt.$$

When $t = s$, the norm of the tangent, $|\dot{\mathbf{X}}| = \sqrt{\dot{x}_1^2 + \dot{x}_2^2 + ... + \dot{x}_n^2} = 1$. $\qquad \square$

With our new investigation that eq.[4.11] is not parameterised in arclength, the set $\mathbf{S} = \{\frac{1}{N}, \frac{2}{N}, ..., \frac{(N-1)}{N}\}$ does not correspond to equal distant points on the filament, nor that the filament length remains constant for varying t. Nonetheless, the mapping between the the parameter s in [4.11] and the real arclength can be found by solving for s_{n+1} in the equation

$$|\mathbf{x}_{cilia}(s_n, t) - \mathbf{x}_{cilia}(s_{n+1}, t)| = \Delta L, \tag{4.17}$$

starting with $s_0 = 0$. The solution set $\mathbf{S}' = \{s_1, ..., s_{n-1}\}$ now expresses points of constant separation on the analytic curve, and is used to evaluate $\kappa_{\hat{\mu}}$. eq.[4.17] is solved using numerical bisection method.

4.4.2 Rotating the base segment

The orientation of the base segment is prescribed as boundary condition, and is not affected by the preferred curvatures. In order to achieve the correct shape described in eq.[4.11], The base segment needs to be treated separately. In practise, we update orientation constraint on the base segment over time. Denote $\zeta(t)$ the angle formed by $\mathbf{g}_1$ and point $\mathbf{x}_{cilia}(s_1, t)$ on the analytic curve,

$$\zeta(t) = atan\left(\frac{\xi^{(2)}(s_1, t)}{\xi^{(1)}(s_1, t)}\right). \tag{4.18}$$

The orientation of the base segment should be updated by the analytic angle difference $\Delta\zeta(t+\Delta t) = \zeta(t + \Delta t) - \zeta(t)$ between two consecutive frames. Benefit from the simplicity of planer motion, without lost of generality the corresponding Lie algebra element $\mathbf{u}$ can be expressed by a single basis vector only, and in our case is given by

$$\mathbf{u}(t) = \Delta\zeta(t)\hat{\nu}(t). \tag{4.19}$$

The orientation of the base segment is then updated using eq.[4.7]. eq.[4.19] is applicable even when the filament is placed on the spherical body in section.6.

4.5 Simulation

In this section, the behaviour of a single tethered filament simulation is examined. For all simulations, the number of segments N in each filament is 20. Position and orientation constraints are applied to the base segment, according to section4.4.2. The time step length is set to a fixed value $\Delta t = 100$. This value will cooperate with beat frequency values lower than 0.01, by allowing at least 100 time steps per beating period.

As discussed earlier, the relaxation of filament to the equilibrium shape requires a finite time to complete, and thus the simulated filament will only achieve the shape in eq.[4.11] in the limit of low beat frequency ω. We examined the effect of varying ω. The difference between the simulation shape and the analytic shape is quantified by a dimensionless quantity η which is defined as the averaged distance between all counterpart simulated and analytic segments, divided by the total length of the filament.

Four simulations of $\omega = 2\pi \times 10^{-3} rad\ s^{-1}, \omega = 2\pi \times 10^{-4} rad\ s^{-1}, 2\pi \times 10^{-5} rad\ s^{-1}$ and $2\pi \times 10^{-6} rad\ s^{-1}$ were investigated, yielding $\eta = 0.41, 0.104, 0.013$ and 0.0032 respectively. The filament shapes during one beat period are shown in Fig.4.2. On the graphs, data points of 20 time instances are plotted. The blue symbols represent the simulated positions of segments, and the blue curves indicate the filament formed by blue symbols. The red symbols represent the evaluations of eq.[4.11] using the set $\mathbf{S}'$ as explained in session4.4.1, thus they correspond to points of constant separation
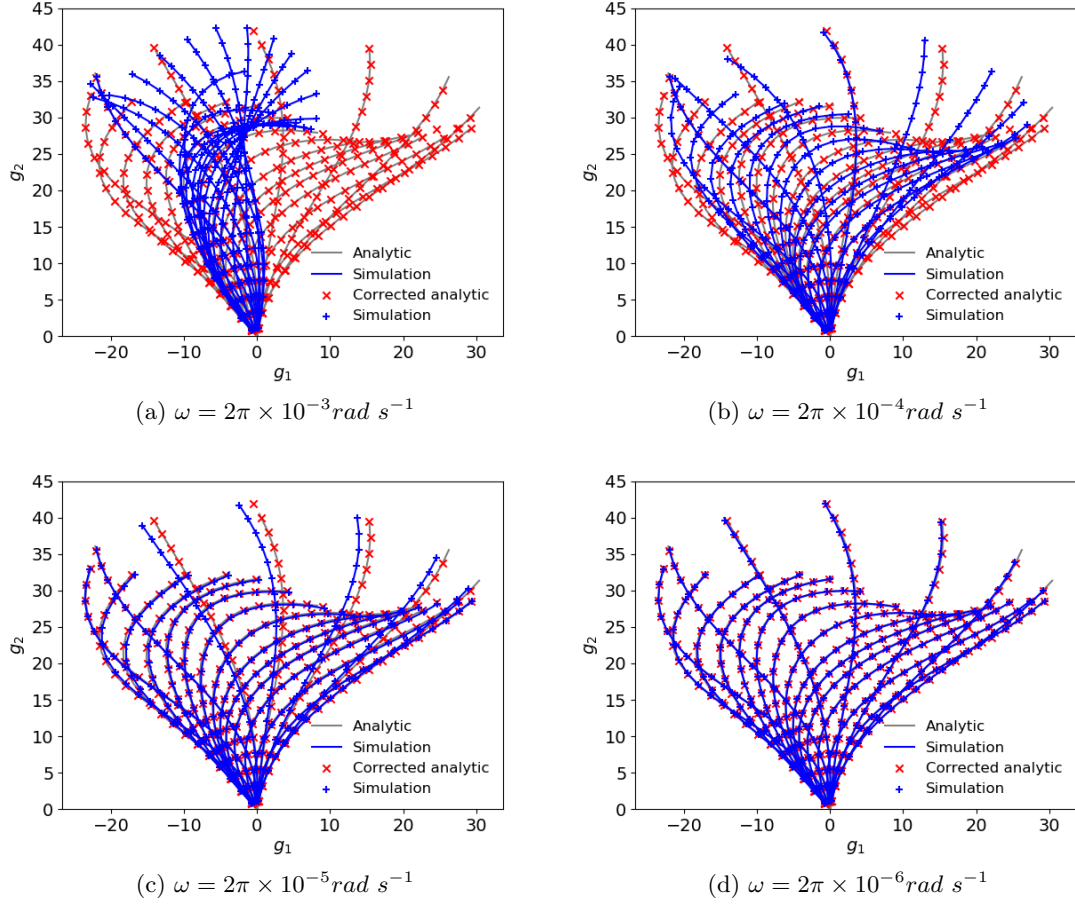
Figure 4.2: Numerical results of a single tethered filament motion during one period. Blue curves and symbols express numerical results, while red symbols are the theoretical positions of each segment. Grey curves represent the scaled analytic function eq.[4.11] with $s \in [0,1]$.

and are expected to coincide with the segments (blue symbols). The grey curves represent the evaluations of eq.[4.11] using $s \in [0,1]$, and they are plotted for comparison purposes. Note that the grey curves sometimes extend beyond, and sometimes does not reach the end segment (red symbols), which is the evidence that the filament described by eq.[4.11] is not of constant length, nor parameterised in arclength.

The result shows that as ω decreases, the simulated shape gradually captures the analytic function. As we explained earlier, the analytic function defines the equilibrium shape of the simulated filament, while in practise the relaxation process requires a finite time to complete. If the beat frequency is fast, the equilibrium changes rapidly, and the simulated filament is always in a state pursuing the equilibrium shape, in which case it may never reach a shape close to the defined equilibrium shape (see Fig.4.2a). However, when $\omega = 2\pi \times 10^{-6} rad\ s^{-1}$ or lower, the simulated shape is close to be identical to the analytic function eq.[4.11].

Chapter 5

Ciliated swimmer models

5.1 The ciliated swimmer by Westwood

In the PhD thesis of Timothy Westwood[Wes20], tethered filaments are attached to a rigid spherical cell body that is free to move in a fluid. The rigid body is constructed based on the multiblod method[UKD+16][SUPD17], where the surface of the body is decomposed into a collection of discrete blobs of finite size, each with position $\mathbf{x}_n$ and subject to a force λ_n.

Each blob is treated as a finite sized sphere in a fluid, and the velocity is

$$\mathbf{v}_n = \mathbf{v}_n^\infty + \sum_{m=1}^{N_{blob}} \mathbf{M}_{nm}\lambda_m, \tag{5.1}$$

where $\mathbf{v}_n^\infty$ is the velocity induced by any external particles other than the rigid body the blob belongs to, i.e. the filament segments. The latter term represents the interaction between blobs, and can be viewed as a simplifeid version of eq.[2.14] without rotation. In the existing model, $\mathbf{M}$ is given by the RPY method as in section2.6. Denote the rigidbody position with $\mathbf{X}_{body}$, transnational velocity $\mathbf{V}_{body}$ and rotation velocity $\mathbf{\Omega}_{body}$, all surface blob has a velocity constraint to keep constant relative postion to the whole rigid body.

$$\mathbf{v}_n = \mathbf{V}_{body} + \mathbf{\Omega}_{body} \times (\mathbf{x}_n - \mathbf{X}_{body}). \tag{5.2}$$

The constraint can be satisfied by treating λ_n as the Lagrange multipliers. Since the rigid body constraints cannot induce a net force or torque on the body, these Lagrange multipliers must satisfy

the force and torque balances

$$\mathbf{F}_{body} = \sum_{m=1}^{N_{blob}} \lambda_m, \tag{5.3}$$

$$\mathbf{T}_{body} = \sum_{m=1}^{N_{blob}} (\mathbf{x}_n - \mathbf{X}_{body}) \times \lambda_m, \tag{5.4}$$

where F_{body} and T_{body} are the total forces on the body. In the filament-body system, force and torque balances must be satisfied, and thus F_{body} and T_{body} are equal to the opposite total forces and torques on all segments in all filaments,

$$-\mathbf{F}_{body} = \sum_{n}^{segments} \mathbf{F}_n, \tag{5.5}$$

$$-\mathbf{T}_{body} = \sum_{n}^{segments} (\mathbf{T}_n + (\mathbf{x}_n - \mathbf{X}_{body}) \times \mathbf{F}_n). \tag{5.6}$$

It can be viewed that the motion of the whole swimmer is solely originated from the internal moment and stress in the filaments, without introducing any external source of force.

The system of equations can be written as

$$\mathbf{K} \begin{pmatrix} \mathbf{V}_{body} \\ \mathbf{\Omega}_{body} \end{pmatrix} = \mathbf{v}^\infty + \mathbf{M}\lambda, \tag{5.7}$$

$$\mathbf{K}^T \lambda = \begin{pmatrix} \mathbf{F}_{body} \\ \mathbf{V}_{body} \end{pmatrix}, \tag{5.8}$$

where un-subscripted vectors contain the corresponding quantities for all blobs, and $\mathbf{K}$ is given by

$$\mathbf{K} = \begin{pmatrix} \mathbf{I} & [\times(\mathbf{x}_1 - \mathbf{X}_{body})] \\ \vdots & \vdots \\ \mathbf{I} & [\times(\mathbf{x}_{N_{blob}} - \mathbf{X}_{body})] \end{pmatrix}, \tag{5.9}$$

with $[\times\mathbf{v}]$ being the skew-symmetric matrix such that $[\times\mathbf{v}]\mathbf{x} = \mathbf{x} \times \mathbf{v}$ and $[\mathbf{v}\times] = -[\times\mathbf{v}] = [\times\mathbf{v}]^T$.

This can be reorganised into a single saddle-point system

$$\begin{pmatrix} \mathbf{M} & -\mathbf{K} \\ -\mathbf{K}^T & \mathbf{0} \end{pmatrix} \begin{pmatrix} \lambda \\ \begin{pmatrix} \mathbf{V}_{body} \\ \mathbf{\Omega}_{body} \end{pmatrix} \end{pmatrix} = \begin{pmatrix} -\mathbf{v}^\infty \\ -\begin{pmatrix} \mathbf{F}_{body} \\ \mathbf{T}_{body} \end{pmatrix} \end{pmatrix} \tag{5.10}$$

In practise, the velocities $\mathbf{v}_n^\infty$ of surface blobs due to the force and torque on the filaments are evaluated, giving $\mathbf{V}_{body}$ and $\mathbf{\Omega}_{body}$. The system eq.[5.10] is then solved using a custom-written

GMRES implementation by Saad and Schultz[SS86]. Given the forces λ on the blobs, the velocities of the segments can now be solved for.

The motion is then solved using numerical time-integration methods, i.e. the time is discretised into small time steps. In each time step physical quantaties of all segments and blobs are calculated and used to update the system.

All analysis in Chapter.6 is based on the computational multiblob model by Timothy Westwood[Wes20].

5.2 The ciliated swimmer by Ishikawa

In the recent research of Ito *et al.*[IOI19] they analysed the motion of a ciliated swimmer using boundary element–slender-body coupling method. Though different in details, both models by Westwood and Ito *et al.* are based on discrete point evaluations on the ciliate. A brief introduction to their methods is given here.

In their model the cilia with prescribed motion[4.11] are attached to a rigid sphere. The flow fields induced by the cilia motion are given by the boundary integral equation eq.[2.11] and slender-body theory, which is provided in Appendix.C. The cell body and cilia are discretised using boundary element method. Denote $\mathbf{q}$ the viscous traction on the cell body, $\mathbf{f}$ the stress density along the cilia, N_c the total number of point evaluation on cilia and N_b the total number of point evaluation on the cell body. The point evaluations form a representation of the velocity on the cilia,

$$[\mathbf{v^c}] = [\mathfrak{J}^{cb}][\mathbf{q}] + [\mathfrak{J}^{cc}][\mathbf{f}], \tag{5.11}$$

and the velocity on the cell body

$$[\mathbf{v^b}] = [\mathfrak{J}^{bb}][\mathbf{q}] + [\mathfrak{J}^{bc}][\mathbf{f}], \tag{5.12}$$

where $[\mathfrak{J}^{cb}]$, $[\mathfrak{J}^{cc}]$, $[\mathfrak{J}^{bb}]$ and $[\mathfrak{J}^{bc}]$ are $3N_c \times 3N_b$, $3N_c \times 3N_c$, $3N_b \times 3N_b$, $3N_b \times 3N_c$ matrices derived from the expression in Appendix.C. Similarly, the point and torque free condition can be written as

$$[\mathbf{F}^b][\mathbf{q}] + [\mathbf{F}^c][\mathbf{f}] = [\mathbf{0}], \tag{5.13}$$

$$[\mathbf{T}^b][\mathbf{q}] + [\mathbf{T}^c][\mathbf{f}] = [\mathbf{0}], \tag{5.14}$$

. The point evaluations must also satisfy a velocity constraint,

$$\begin{cases} \mathbf{v}(\mathbf{x}) = \mathbf{V} + \boldsymbol{\Omega} \times \hat{\mathbf{r}}(\mathbf{x}) & \mathbf{x} \in cell\ body \\ \mathbf{v}(\mathbf{x}) = \mathbf{V} + \boldsymbol{\Omega} \times \hat{\mathbf{r}}(\mathbf{x}) + \mathbf{v}^{cilia}(\mathbf{x}) & \mathbf{x} \in cilia \end{cases}. \tag{5.15}$$

Combining the equations[5.11][5.12][5.13][5.14] and boundary condition[5.15], the system is

$$
\begin{bmatrix}
\mathfrak{J}^{bb} & \mathfrak{J}^{bc} & \mathbf{V}^b & \mathbf{A}^b \\
\mathfrak{J}^{cb} & \mathfrak{J}^{cc} & \mathbf{V}^c & \mathbf{A}^c \\
\mathbf{F}^b & \mathbf{F}^c & \mathbf{0} & \mathbf{0} \\
\mathbf{T}^b & \mathbf{T}^c & \mathbf{0} & \mathbf{0}
\end{bmatrix}
\begin{bmatrix}
\mathbf{q} \\
\mathbf{f} \\
\mathbf{V} \\
\boldsymbol{\Omega}
\end{bmatrix}
=
\begin{bmatrix}
\mathbf{0} \\
\mathbf{v}^{\mathbf{cilia}} \\
\mathbf{0} \\
\mathbf{0}
\end{bmatrix},
\tag{5.16}
$$

solving which will give the velocities at all point evaluations, and the system can be updated using second-order Runge–Kutta method.

Swimming velocities and energy dissipations of ciliates of different metachronal wave patterns have been studied in their paper. A comparison is also made between their ciliated swimmer and a squirmer, yielding quantatatively consistent swimming speeds.

30

Chapter 6

Simulation

We modified the multiblob model in section.5.1 to construct a spherical ciliate following the setups in Ito *et al.*[IOI19]. In consideration of the shape of the body, it is natural to use spherical polar coordinate system (r, θ, ϕ) which correspond to radial distance, polar angle, and azimuthal angle respectively. The cilia were located at the vertices of triangular meshes made by dividing an icosahedron (see Fig.6.1), with one of the vertice of the original icosahedron being the north pole $(\theta = 0)$ of our coordinate system. For each cilium at $\mathbf{x}_c$ on the body, the prescribed motion is described in eq.[4.11], with the basis vectors $\mathbf{g}_1$ and $\mathbf{g}_2$ aligned with the basis vectors of spherical coordinates $\hat{\theta}(\mathbf{x}_c)$ and $\hat{\mathbf{r}}(\mathbf{x}_c)$ respectively. Thus, the motion of filament is confined in the $r - \theta$ plane.

| icosahedron | divide 1 time | divide 2 times |
| vertex = 12 | vertex = 42 | vertex = 162 |
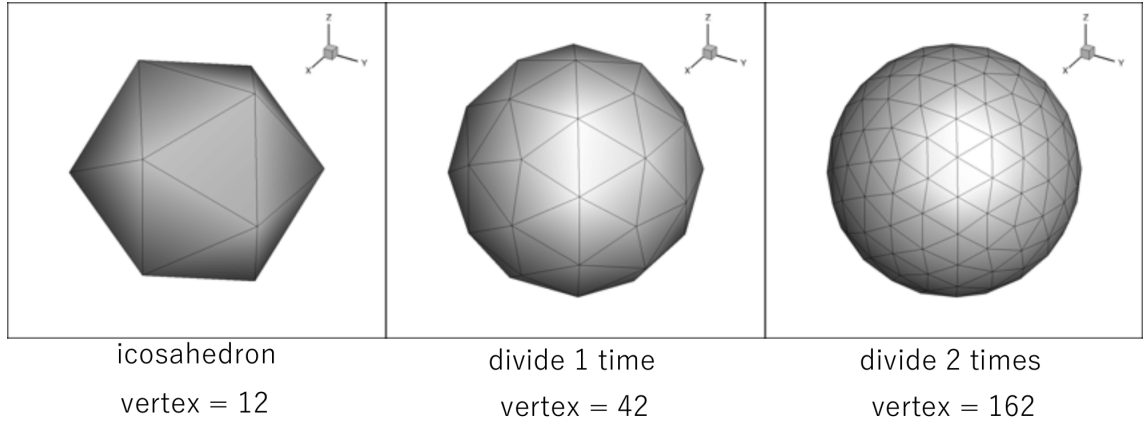
Figure 6.1: Triangular meshes from dividing an icosahedron. Image credit: Ito *et al.*[IOI19]

For all computations, the beat frequency $\omega = 2\pi \times 10^{-4} rad\ s^{-1}$ and the time step length $\Delta t = 100$ are used, yielding a period $T = 10^4$ and time step number per period $\gamma = 100$, which corresponds to the ciliary pattern shown in Fig.4.2b. The radius a_0 of the body is set to $a_0/L = 3.0$, and the aspect ratio of filament is $1/44$. There are 160 filaments, each of which comprises of 20 segments, and the total number of surface blobs is 7000. We assume that all cilia exhibited identical beat

frequencies but with different initial ciliary beat phase $\psi^0(\theta, \phi)$ that depends on its relative position on the body,

$$\psi^0/2\pi = sin(k\theta/2) + sin(q\phi/4), \tag{6.1}$$

where k and q are the wavenumber parameters.

6.1 Effect of varying k

We first set the wavenumber $q = 0$. The ciliary beat phase now depends on θ only, and the swimmer can be viewed as axis-symmetric at large number of cilia. The wavenumber k determines the metachronal wave patterns to be either a symplectic metachronal wave (k=-1) where, the beat direction is the same as that of wave transmission; or an antiplectic metachronal wave (k=1) where the two directions are opposed. The motions of $k = 0$ and $k = 1$ from our numerical results are illustrated in Fig.6.2 and Fig.6.3 respetively.[1]
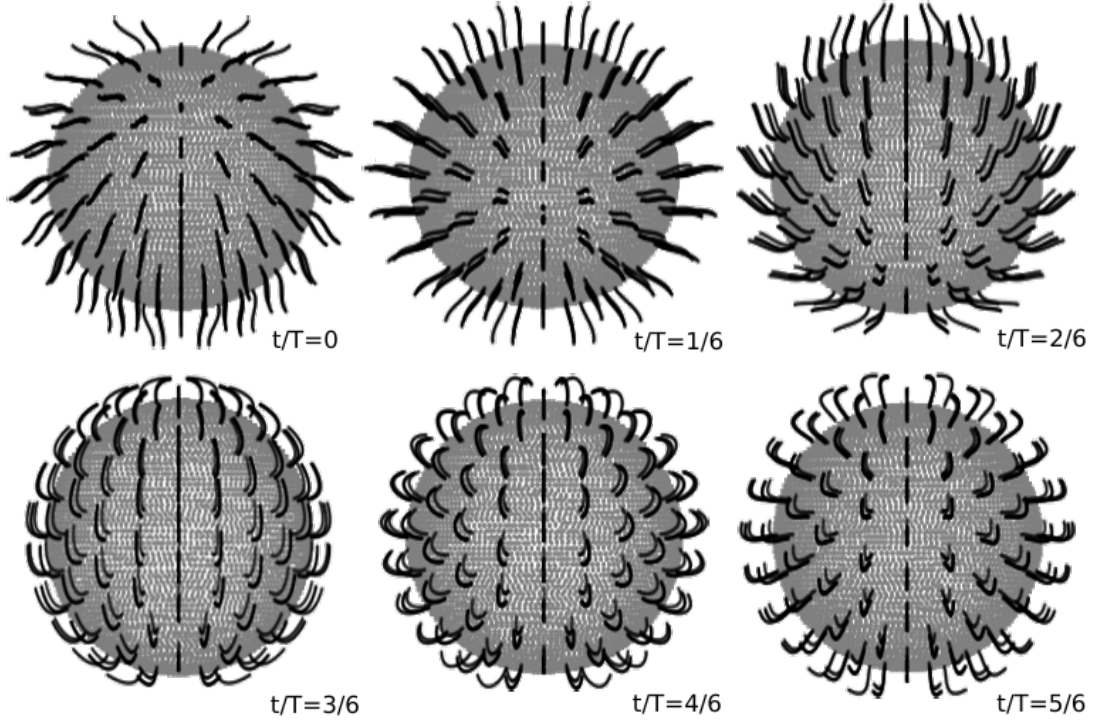
Figure 6.2: Swimming gaits of the ciliate during one period (k=0).

As mentioned in section5.1, the motion of surface blobs are calculated from the force and torque on the filaments through RPY mobility matrix. The body velocity is then deduced from the velocities of the surface blobs through the constraint eq.[5.2]. In our computation, the direction of $\mathbf{g}_1$ is set towards the north pole ($\theta = 0$), thus the ciliate swims towards the south pole ($\theta = \pi$), or the negative z-direction. The swimming speed of varying k during one beat period is shown in Fig.6.4a, compared with the results of Ito *et al.*[IOI19] in Fig.6.4b.

[1]Due to time discretisation, the ratio t/T is close to, but may not be the exact value shown in the figures.

Figure 6.3: Swimming gaits of the ciliate during one period (k=1).

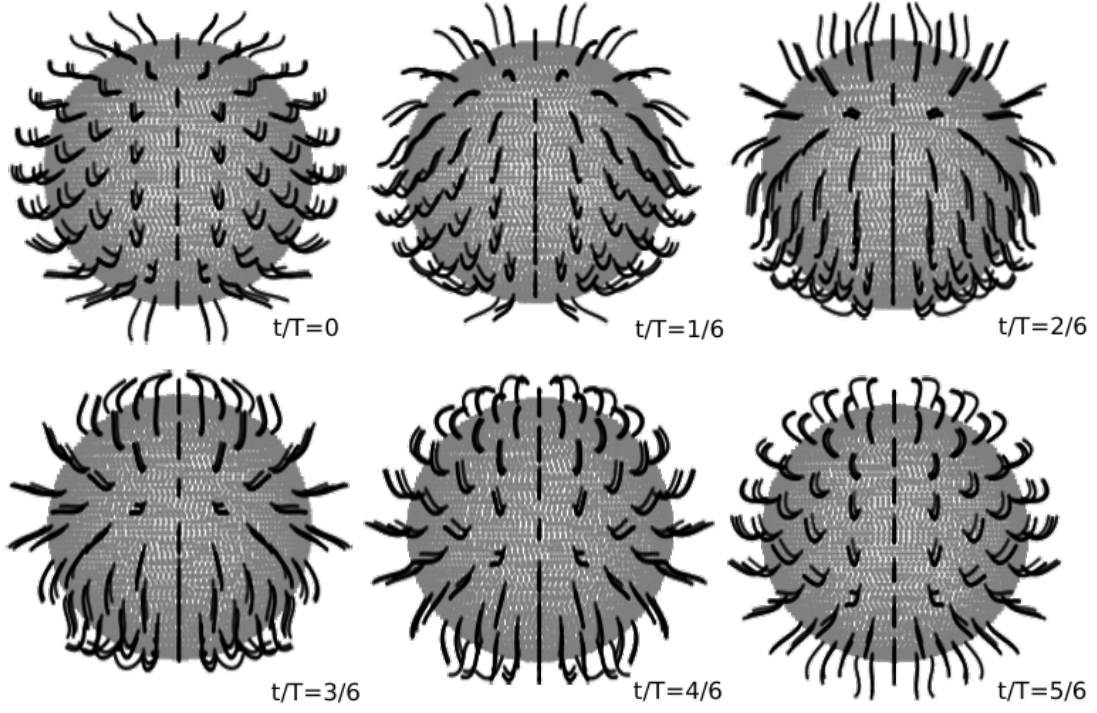In Fig.6.4 there exist obvious differences between the two results, but curves of same k in the two graphs still exhibit similar general patterns. We observed phase differences between all curves in the two graphs, which could potentially be caused by the delay of relaxation process as discussed in section4.5. In our simulations, we were restricted by the expensive computation cost and time constraint, and only able to perform analysis based on a relatively high beat frequency ($\omega = 2\pi \times 10^{-4} rad\ s^{-1}$), which corresponds to Fig.4.2b in section4.5. We observed that the analytic shape is not fully captured by the simulated filament at this frequency. When the filament is experiencing fast movement, i.e. moving in the positive $\mathbf{g}_1$ direction as shown in Fig.4.2b, a significant delay is observed, since the relaxation of filament requires additional time to complete. This effect potentially explains the obvious phase difference of the two results in Fig.6.4, as well as contributes to the speed value differences. However, since all cilia are delayed by the same amount, the delay effect will not change the inter-cilia phase differences. Therefore, the wavenumber k still determines the metachronal wave pattern, i.e. $k = 1$ corresponds to an antiplectic metachronal wave, and $k = -1$ a symplectic metachronal wave. This explains why the two models exhibit similar patterns of time changes of speed for the same k.

The relation between average speed during one beat period and k is shown in Fig.6.5. Both results shown that an antiplectic metachronal wave ($k = 1$) is optimal in swimming speed, while a symplectic metachronal wave ($k = -1$) is least efficient.

Other factor could potentially cause difference of the two models. For example, the motions of

(a) (b)
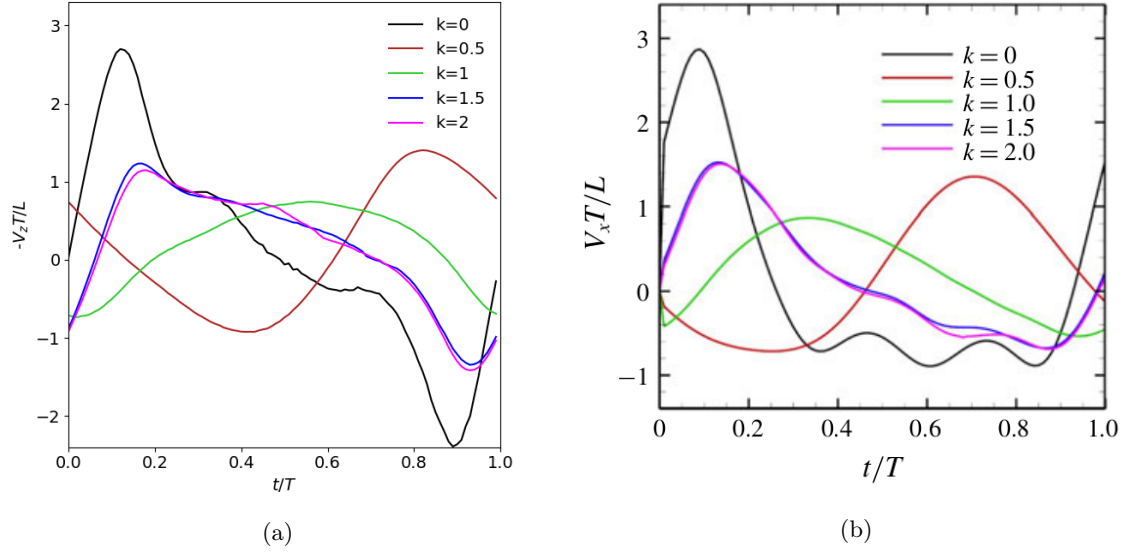
Figure 6.4: Time changes of ciliate swimming speed during one period. Fig.6.4a: numerical results of our simulation data. Fig.6.4b: Image taken from Ito *et al.*[IOI19]. The scales of axes are set equal in the two figures. The general patterns for different k are similar, while apparent differences are also observed.

discretised particles are solved using different methods. In our model, the mobility matrix is given by RPY method eq.[2.24], and the body speed is calculated through Multi-blob rigid body construction. While in Ito *et al.* slender-body theory is applied, and the body is discretised using Boundary element method. However, the difference in using these two evaluation methods remains unclear.

Figure 6.5: Average velocities changes with k. The blue curve represents our simulation result; the black curve is taken from Ito *et al.*[IOI19]. Both results show that the optimal speed corresponds to antiplectic metachronal waves ($k = 1$).

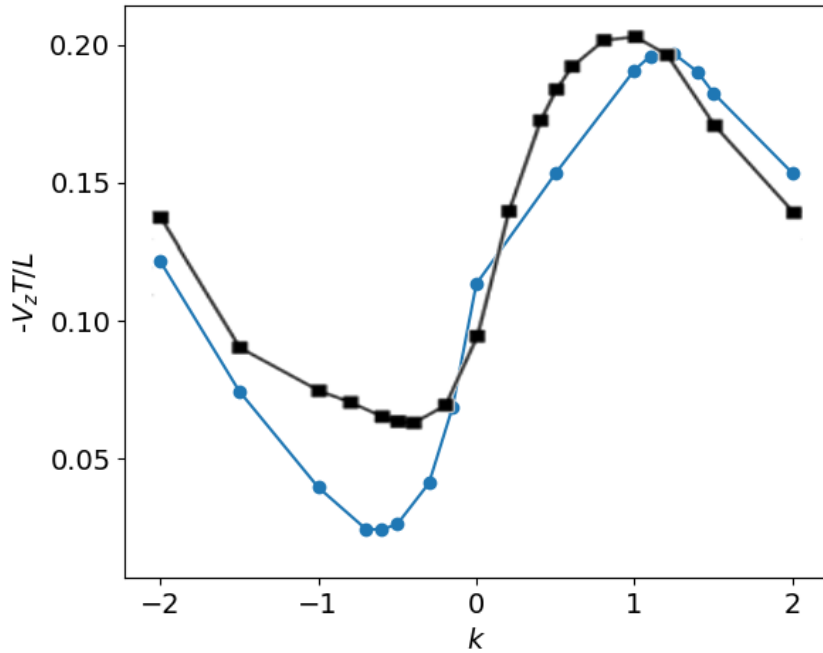## 6.2 Comparison with the squirmer model

The difference between our model and that of Ito *et al.*, however, does not hinder us to compare our model with the Lighthill-Blake squirmer. In specific, we chose a spherical envelope that is just outside the cilia, and evaluated the flow velocity at discretised points on the envelope. The point evaluations are then used to fit eq.[3.1] using a least-squares method to approximate the squirming sets $\mathbf{A}_n$ and $\mathbf{B}_n$. The swimming speed of the squirmer is then given by $U = 1/3(2B_1 - A_1)$.

In practise, the radius of the sperical envelope is set equal to the farthest distance from all point evaluations to the ciliate center, added by an offset $\epsilon = 0.05L$ to avoid singularities in calculation. The forces and torques on all segments and blobs are treated as point forces and torques at their positions. Under the force and torque free condition, the fluid experiences the opposite point forces and torques at the same positions. Each point force and torque generate a stokeslet (eq.[2.7]) or rotlet (eq.[2.8]) flow, and the sum of these flows could be viewed as an approximation of the flow field induced by the whole swimmer, due to the linearity of Stokes equation. This method is also a discrete version of the single-layer potential boundary integral method[2.11].
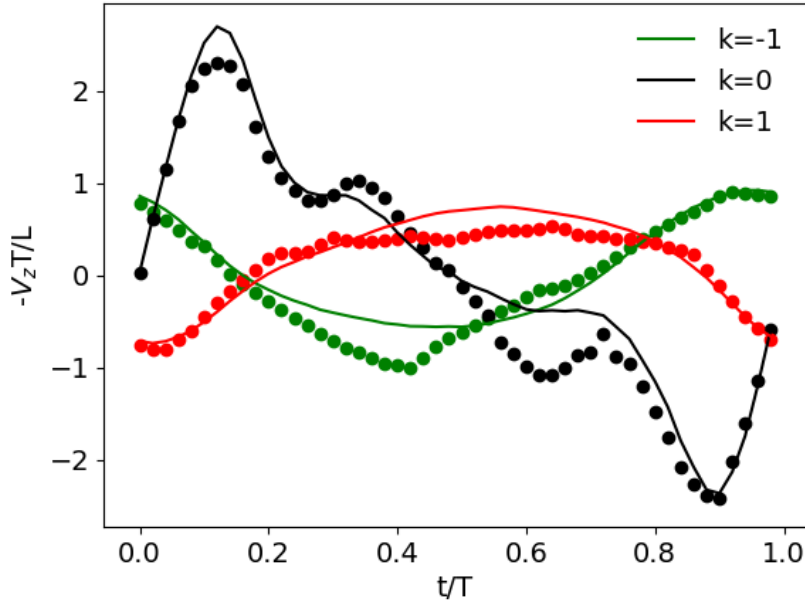
Figure 6.6: Velocity comparison with the squirmer. Solid lines represent numerical results, while symbols are from the theory, calculated using the fitted squirming sets.

For each time frame, the flow field is evaluated at azimuthal angles $\phi = 0$, $\frac{1}{3}\pi$ and $\frac{2}{3}\pi$. For each ϕ, 12 equally spaced $\theta \in [\frac{1}{13}\pi, \frac{12}{13}\pi]$ are chosen, yielding total 36 point evaluations on the envelope per time frame. The velocities are averaged in the ϕ-direction.

We compared the time changes in the body speed and the fitted squirmer speed in Fig.6.6. The curves represent the body swimming speed, while scatters the squirmer speed. Overall, the two speeds are consistent, while the mismatches could be from the flow field approximation we made.

6.3   Oblique metachronal wave

In nature, cilia can exhibit non-axisymmetric motions, giving an oblique metachronal wave. We investigated this effect by setting a non-zero wavenumber q, corresponding to matachronal wave propagating in the ϕ-direction. In simulation, a dexioplectic wave propagation (wave is directed to the right of the effective beat) is established by setting $q = 1$ and $k = 1$. The trajectory of the body over 10 beat period is show in Fig.6.7. A right-handed helical trajectory is observed, which qualitatively agreed with Ito *et al.*[IOI19].
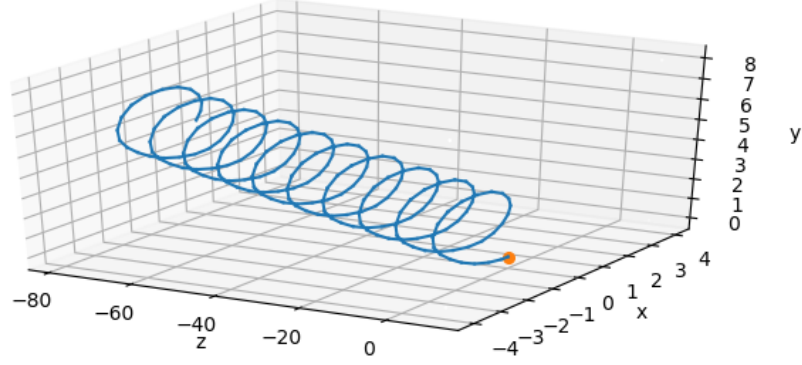

Figure 6.7: Trajectorie of ciliate with dexioplectic metachronal wave (k=1.0, q=1.0). The starting position is indicated by the orange dot on the graph.

Chapter 7

Conclusion and outlook

We adapted the prescribed ciliary motion in the ciliate model of Ito *et al.* to a single instability driven filament model of Westwood. When the beat frequency $\omega < 2\pi \times 10^{-6} rad\ s^{-1}$, the flexible filament model achieves the shape defined by the mathematical formula. The modification is further applied to the ciliate model of Westwood, with a relatively large beat frequency $\omega = 2\pi \times 10^{-4} rad\ s^{-1}$. Despite the analytic shape is not fully captured by each cilium, the speed profiles for different metachronal wave patterns are consistent between the two ciliate models. We verified that antiplectic metachronal wave was optimal in the swimming speed for a spherical ciliate. By treating the forces and torques on all particles as point sources, using force free condition we evaluated the flow velocities on the squirmer envelope. The theoretical squirmer speed is then fitted using data, and quantitatively agreed with our numerical results. We thus conclude that the speed of a ciliate can be predicted by a squirmer.

In the analysis we have done, the ciliate cell considered was spherical. In nature, however, micro-organisms assume various forms. Multi-blob method is capable to resolve potentially complex surface geometries of rigid particles. Thus, the existing method can be extended to analyse swimmers of complex shapes.

On completing this thesis only the swimming speed is compared with the squirmer model. However, it is possbile to apply the RPY method in investigation of the interactions between ciliates in the future.

Appendix A

C. Rheinardtii squirming coefficients

a_0	a_1	a_2	b_1	b_2
49.56	-32.39	-12.76	122.24	-8.44

Table A.1: Magnitudes of the Fourier modes used to describe $B_1(t)$ in rad s^{-1} . [GA14]

c_0	c_1	c_2	c_3	s_1	s_2	s_3
4.5347	64.053	-84.7192	-10.4545	91.4529	-92.6420	-5.9849

Table A.2: Magnitudes of the Fourier modes used to describe $B_2(t)$ in rad s^{-1} . [DKPC15]

φ_{c_1}	φ_{c_2}	φ_{c_3}	φ_{s_1}	φ_{s_2}	φ_{s_3}
1.7373	3.5761	-0.9154	0.1666	2.0054	-1.7125

Table A.3: Phases of the Fourier modes used to describe $B_2(t)$ in rad. [DKPC15]

Appendix B

Filament beating coefficient

$\left[A_{mn}^{(1)}\right]$	n	0	1	2	3	$\left[A_{mn}^{(2)}\right]$	0	1	2	3
	1	-0.654	0.393	-0.097	0.079		1.895	-0.018	0.158	0.010
m	2	0.787	-1.516	0.032	-0.302		-0.552	-0.126	-0.341	0.035
	3	0.202	0.716	-0.118	0.142		0.096	0.263	0.186	-0.067
$\left[B_{mn}^{(1)}\right]$	n	1	2	3		$\left[B_{mn}^{(2)}\right]$	1	2	3	
	1	0.284	0.006	-0.059			0.192	-0.050	0.012	
m	2	1.045	0.317	0.226			-0.499	0.423	0.138	
	3	-1.017	-0.276	-0.196			0.339	-0.327	-0.114	

Table B.1: Coefficients for ciliary beating, taken from [IOI19]

Appendix C

Boundary integral equation with slender-body theory

The original derivations for this appendix can be found in Ito *et al.*[IOI19].

Denote $\mathbf{q}$ the traction force on the cell body, and $\mathbf{f}$ stress density along cilia. Velocity on the ith cilia given by the slender-body-boundary integral coupling method:

$$
\begin{aligned}
\mathbf{v}_c(\mathbf{x}) = & -\int_{cell} \mathbf{G}(\mathbf{x},\mathbf{y}) \cdot \mathbf{q}(\mathbf{y}) dS(\mathbf{y}) - \mathbf{\Lambda}(\mathbf{x}) \cdot \mathbf{f}(\mathbf{x}) \\
& -\int_{cilia} [\mathbf{G}(\mathbf{x},\mathbf{y}) \cdot \mathbf{f}(\mathbf{y}) + \mathbf{K}(\mathbf{x},\mathbf{y}) \cdot \mathbf{f}(\mathbf{x})] ds_i(\mathbf{y}) \\
& -\sum_{j\neq i}^{N} \int_{cilia} [\mathbf{G}(\mathbf{x},\mathbf{y}) + \mathbf{W}(\mathbf{x},\mathbf{y})] \cdot \mathbf{f}(\mathbf{y}) ds_j(\mathbf{y})
\end{aligned}
\tag{C.1}
$$

and outside the cilia (on the body):

$$
\begin{aligned}
\mathbf{v}_b(\mathbf{x}) = & -\int_{cell} \mathbf{G}(\mathbf{x},\mathbf{y}) \cdot \mathbf{q}(\mathbf{y}) dS(\mathbf{y}) \\
& -\sum_{j\neq i}^{N} \int_{cilia} [\mathbf{G}(\mathbf{x},\mathbf{y}) + \mathbf{W}(\mathbf{x},\mathbf{y})] \cdot \mathbf{f}(\mathbf{y}) ds_j(\mathbf{y}),
\end{aligned}
\tag{C.2}
$$

where $\mathbf{G}(\mathbf{x},\mathbf{y})$ is the Oseen tensor, $\mathbf{\Lambda}(\mathbf{x})$ and $\mathbf{K}(\mathbf{x},\mathbf{y})$ are local operators of the slender-body theory, which are defined by

$$
\mathbf{\Lambda}(\mathbf{x}) = \frac{1}{8\pi\mu} \left[c \left[\delta_{ij} + t_i(\mathbf{x})t_j(\mathbf{x}) \right] + 2 \left[\delta_{ij} - t_i(\mathbf{x})t_j(\mathbf{x}) \right] \right],
\tag{C.3}
$$

and

$$
\mathbf{K}(\mathbf{x},\mathbf{y}) = -\frac{1}{8\pi\mu} \frac{\delta_{ij} + t_i(\mathbf{x})t_j(\mathbf{x})}{|s(\mathbf{x}) - s(\mathbf{y})|}
\tag{C.4}
$$

where $\mathbf{t}$ is the unit tangential vector of the cilium, and $c = -ln(\epsilon^2 e)$, $\epsilon = a_{cilia}/L$ the aspect ratio of a cilium and $s(\mathbf{x})$ the arclength along the centerline.

The slender-body kernel $\mathbf{w}$ is defined by

$$\mathbf{W}(\mathbf{x}, \mathbf{y}) = \frac{1}{8\pi\mu} \frac{(\epsilon L)^2}{2} \left(\frac{\delta_{ij}}{r^3} - 3\frac{r_i r_j}{r^5} \right). \tag{C.5}$$

The force-free and torque-free conditions are

$$\int_{cell} \mathbf{q} dA = \sum_{i=1}^{N} \int_{cilia} \mathbf{f} ds_i = 0 \tag{C.6}$$

$$\int_{cell} \mathbf{q} \times \hat{\mathbf{r}} dA = \sum_{i=1}^{N} \int_{cilia} \mathbf{f} \times \hat{\mathbf{r}} ds_i = 0 \tag{C.7}$$

Bibliography

[Bla71]   J. R. Blake. A spherical envelope approach to ciliary propulsion. *Journal of Fluid Mechanics*, 46(1):199–208, 1971.

[CW75]   A. T. Chwang and T. Y. Wu. Hydromechanics of low-reynolds-number flow. part 2. singularity method for stokes flows. *Journal of Fluid Mechanics*, 67(4):787–815, 1975.

[DKPC15]   B. Delmotte, E. E. Keaveny, F. Plouraboué, and E. Climent. Large-scale simulation of steady and time-dependent active suspensions with the force-coupling method. *Journal of Computational Physics*, 302:524 – 547, 2015.

[EL12]   C. Eloy and E. Lauga. Kinematics of the most efficient cilium. *Physical Review Letters*, 109(3), Jul 2012.

[FB86]   G. R. Fulford and J. R. Blake. Muco-ciliary transport in the lung. *Journal of Theoretical Biology*, 121(4):381 – 402, 1986.

[GA14]   S. Ghose and R. Adhikari. Irreducible representations of oscillatory and swirling flows in active soft matter. *Physical Review Letters.*, 112:118102, Mar 2014.

[GJG10]   J. S. Guasto, K. A. Johnson, and J. P. Gollub. Oscillatory flows induced by microorganisms swimming in two dimensions. *Physical Review Letters.*, 105:168102, Oct 2010.

[GMP11]   É. Guazzelli, J. F. Morris, and S. Pic. *A Physical Introduction to Suspension Dynamics*. Cambridge Texts in Applied Mathematics. Cambridge University Press, 2011.

[IOI19]   H. Ito, T. Omori, and T. Ishikawa. Swimming mediated by ciliary beating: Comparison with a squirmer model. *Journal of Fluid Mechanics*, 874:774–796, 2019.

[ISP06]   T. Ishikawa, M. P. Simmonds, and T. J. Pedley. Hydrodynamic interaction of two swimming model micro-organisms. *Journal of Fluid Mechanics*, 568:119–160, 2006.

[Kea08]   E. E. Keaveny. *Dynamics of structures in active suspensions of paramagnetic particles and applications to artificial micro-swimmers*. PhD thesis, Brown University, January 2008.

[Lig52]   M. J. Lighthill. On the squirming motion of nearly spherical deformable bodies through liquids at very small reynolds numbers. *Communications on Pure and Applied Mathematics*, 1952.

[LP09]   E. Lauga and T. R. Powers. The hydrodynamics of swimming microorganisms. *Reports on Progress in Physics*, 72(9):096601, Aug 2009.

[ML09]   S. Michelin and E. Lauga. The long-time dynamics of two hydrodynamically-coupled swimming cells. *Bulletin of mathematical biology*, 72:973–1005, 12 2009.

[PAY07]   C. M. Pooley, G. P. Alexander, and J. M. Yeomans. Hydrodynamic interaction between two swimmers at low reynolds number. *Physical Review Letters*, 99(22), November 2007.

[Poz92]   C. Pozrikidis. *Boundary Integral and Singularity Methods for Linearized Viscous Flow*. Cambridge Texts in Applied Mathematics. Cambridge University Press, 1992.

[Pur77]   E. M. Purcell. Life at low reynolds number. *American journal of physics*, 45(1):3–11, 1977.

[SS86]   Y. Saad and M. H. Schultz. Gmres: A generalized minimal residual algorithm for solving nonsymmetric linear systems. *SIAM Journal on Scientific and Statistical Computing*, 7(3):856–869, 1986.

[STWK19]   S. Schoeller, A. Townsend, T. Westwood, and E. E. Keaveny. Methods for suspensions of passive and active filaments. *Computational Physics*, 2019.

[SUPD17]   B. Sprinkle, F. B. Usabiaga, N. A. Patankar, and A. Donev. Large scale brownian dynamics of confined suspensions of rigid particles. *The Journal of Chemical Physics*, 147(24):244103, Dec 2017.

[UHOG08]   P. T. Underhill, J. P. Hernandez-Ortiz, and M. D. Graham. Diffusion and spatial correlations in suspensions of swimming particles. *Physical Review Letters*, 100:248101, Jun 2008.

[UKD$^+$16] F. B. Usabiaga, B. Kallemov, B. Delmotte, A. Bhalla, B. Griffith, and A. Donev. Hydrodynamics of suspensions of passive and active rigid particles: a rigid multi-blob approach. *Communications in Applied Mathematics and Computational Science*, 11(2):217–296, Dec 2016.

[Wes20]   T. A. Westwood. *Computational methods for flexible filaments and Brownian suspensions*. PhD thesis, Imperial College London, 2020.

[WMZS13] E. Wajnryb, K. A. Mizerski, P. J. Zuk, and P. Szymczak. Generalization of the rotne–prager–yamakawa mobility and shear disturbance tensors. *Journal of Fluid Mechanics*, 731:R3, 2013.

[ZZDP05] W. L. Zeile, F. Zhang, R. B. Dickinson, and D. L. Purich. Listeria 's right-handed helical rocket-tail trajectories: Mechanistic implications for force generation in actin-based motility. *Cell motility and the cytoskeleton.*, 60(2):121–128, 2005.